ARMA 24–0162

Fracture Characteristics of Shale: Unraveling CO_2-Driven Mechanical Metamorphosis at Microscale

Mahgoub, SA.
Texas A&M University, College Station, Texas, USA
Abedi, S.
Texas A&M University, College Station, Texas, USA

This paper was prepared for presentation at the 58th US Rock Mechanics/Geomechanics Symposium held in Golden, Colorado, USA, 23-26 June 2024. This paper was selected for presentation at the symposium by an ARMA Technical Program Committee based on a technical and critical review of the paper by a minimum of two technical reviewers. The material, as presented, does not necessarily reflect any position of ARMA, its officers, or members. Electronic reproduction, distribution, or storage of any part of this paper for commercial purposes without the written consent of ARMA is prohibited. Permission to reproduce in print is restricted to an abstract of not more than 200 words; illustrations may not be copied. The abstract must contain conspicuous acknowledgement of where and by whom the paper was presented.

ABSTRACT: This study investigates the distinction between unreacted shale samples and those exposed to CO_2-rich brine under elevated temperature (100°C) and pressure (1800 psi) conditions over 28 days. Samples underwent scratch testing under constant loading to ensure independent penetration depth, circumventing variability associated with load-dependent outcomes prevalent in progressive loading methodologies. Vertical hardness profiles revealed significant variations between reacted and unreacted regions, influenced by differential dissolution and precipitation characteristics, while horizontal hardness provided limited insights, particularly in the reacted region where higher tangential forces and deeper scratches indicated greater material compressibility. Distinct scratch path variations were observed, with fractures absent in the ductile reacted region at lower testing forces. The shale samples were sourced from the Eagle Ford Formation, providing insights into the mechanical response of carbonate-rich shale rocks in extreme environments. This research enhances understanding of shale's mechanical properties and material responses under diverse operational conditions, elucidating interactions with influential environmental factors, particularly in CO_2-exposed scenarios. Conducted at a microscale level, this study offers detailed insights into material behavior, crucial for predicting long-term stability of geostructures exposed to reactive brine and potential CO_2 leakage in subsurface reservoirs.

1. INTRODUCTION

The investigation into chemical interactions between carbonate rocks and acidic brine is cruical for understanding complex mechanical and microstructural transformations essential for applications like geostructure stability, CO_2 storage, and energy exploitation. Under elevated pressure and temperature conditions, the equilibrium between injected fluids and rocks undergoes alterations, leading to geochemical responses, especially with the presence of CO_2 as a supercritical phase or in aqueous form (Prakash et al. 2023a; Prakash et al. 2022). In this context, investigating fracture properties becomes essential, aiming to comprehend the development and propagation of fractures within reacted formations to evaluate structural integrity and potential pathways for fluid migration.

Prior geochemical investigations have explored the localized repercussions of CO_2 attacks on rock permeability, shedding light on alterations attributed to carbonate precipitation sealing fractures and pores or the dissolution of diverse minerals (Burnside et al. 2013; Minardi et al. 2021). Shale rocks exposed to acidic brine predominantly undergo carbonate reactions, particularly carbonates dissolution and precipitation (Prakash et al., 2022; Prakash et al. 2023b). Experimental studies on fracture mechanics and mechanical properties have utilized conventional methods such as single edge notched bend, chevron notched beam, three-point bending, and semi-circular bending tests, acknowledging their inherent limitations (Smith & Chowdary, 1975; Bazant and Kazemi, 1990; Helmer et al. 2014; Dubey et al., 2020).

The chemo-mechanical interactions between rock and CO_2-rich brine can induce dissolution and precipitation processes, particularly affecting load-bearing mineral phases such as carbonates, known for their faster reaction kinetics compared to siliceous minerals (Gunter et al., 2000; Pokrovsky et al. 2005; Prakash et al. 2021). Previous investigations employing indentation tests have demonstrated that CO_2-water mixtures can diminish the mechanical properties of rocks by reducing the size of cement bonds (Sun et al. 2016).

In rock mechanics, brittleness is delineated by a range of criteria involving elastic and plastic strains, compression, tensile strength, and post-peak behavior as expounded upon by Hucka and Das (1974) and Meng et al. (2015). Hernandez-Uribe et al. (2017) noted that the scratch brittleness index, defined as the proportion of energy linked to brittle failure to the total energy expended during a scratch, shows a positive correlation with increasing Young's modulus and decreasing Poisson's ratio. However, this relationship may diverge in rocks with distinct porosity and stress-sensitive brittle/ductile behavior, as illustrated by Eagle Ford samples demonstrating a mixture of ductile and brittle failure characteristics.

During scratch testing, under ductile deformation conditions, there may be a disintegration of the matrix material, resulting in the accumulation of grains and powder ahead of the scratch probe and alongside residual scratches, as outlined by Richard et al. (1998, 2012). Plastic flow, characterized by continual deformation, typically does not demonstrate abrupt strain energy release. Nevertheless, with increasing scratch depth, instances of rising transverse force may align with ductile failure occurrences. Notably, brittle and ductile failure modes exhibit distinct transverse force signals. Brittle failure often presents as a conspicuous 'saw-tooth' transverse force response with significant fluctuations, while ductile failure displays a profile with smaller fluctuations (Richard et al. 2012).

In the scope of this study, the chemo-mechanical behavior of cross-sectional carbonate-rich shale exposed to CO_2-rich brine at high pressure and high temperature condition will be explored utilizing a micro-scratch test methodology. The approach involves treating the shale as a composite material attached to a high-performing engineering thermoplastic material (Delrin). Our novel methodology employs scratch testing under constant loading, ensuring precision and independence of penetration depth. This addresses mechanical alterations within reacted and unreacted zones. Additionally, this study explores and discusses fracture patterns in Reacted (Ductile) and unreacted (Brittle) regions. Focused on scratch testing and microscale perspectives, our study characterizes microstructural evolution and chemo-mechanical interactions in a carbonate-rich shale rock, offering insights into chemical reactions and mechanical property changes.

2. EXPERIMENTAL TECHNIQUES

2.1. Material Description

The outcrop rock examined in this study is sourced from Eagle Ford B (EF-B), characterized as a carbonate-rich shale. X-ray diffraction (XRD) analysis delineated its mineralogical composition, with weight proportions of 53.9% calcite, 24.3% quartz, and 8.3% gypsum (Prakash et al. 2022; Prakash et al. 2019). As the shale rocks have complex composition, anisotropic, heterogeneous microstructure, and multi-scale chemo-mechanical behaviour, the samples were tested for different orientations based on how the scratch test is performed with respect to the bedding planes (Kabir et al. 2017; Martogi et al. 2023). The testing protocol included scratch assessments in Divider (parallel to bedding planes) and Arrester (perpendicular to bedding planes) directions. However, short-transverse tests were not conducted due to the risk of compromising the integrity of the reacted surface of our cross-sectional sample. These orientations are explained with accompanying sketches concerning the scratch direction in Fig. 1.

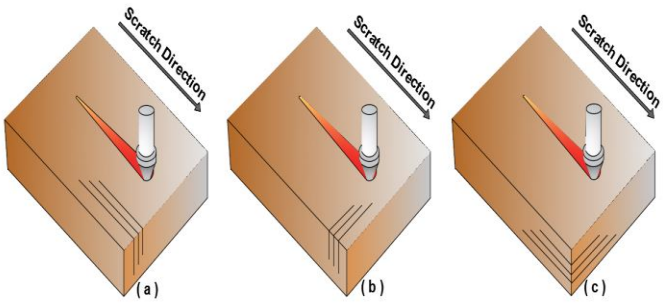

Fig. 1. Scratch orientations; (a) Divider, (b) Arrester, and (c) Short-Transverse.

The rock samples underwent precision cutting into square/ rectangular shapes using a diamond saw, followed by a standard polishing procedure to ensure surface cleanliness and smoothness. This involved initial coarse polishing with a 400-grit abrasive disc to reveal fine details and textures on the rock surface. Subsequent ultrasonic cleaning removed contaminants by immersing the samples in a cleaning solution while subjecting them to high-frequency sound waves. Finally, the surface was refined using finer aluminum oxide pads. Once polished, the rocks were stored for subsequent testing (Martogi et al., 2020). For CO_2-reacted samples, the process involved cutting the samples and placing them inside a batch-type Parr dissolution reactor to investigate fluid-rock reactions. The samples were positioned within a 250 ml Titanium reactor, filled with a 1M NaCl solution, maintaining a liquid-to-solid weight ratio of 19. The temperature was held constant at 100°C, and upon reaching the target temperature, CO_2 was injected through a syringe pump and accumulator until the pressure reached and stabilized at 1800 psi (122.5 atm). These conditions were sustained for a duration of 28 days. Upon completion of the reaction period, a gradual depressurization process was initiated to mitigate the risk of sample spalling. Subsequently, the samples underwent the standard sequence of cutting, grinding, and polishing of the cross-sectional surface. Great attention was paid to securely affix the reacted surface to Delrin to guarantee

the accuracy of scratch test results, considering the vulnerability of the reacted surface to potential damage.

2.2. Scratch Testing

In this study, the scratch tests were carried out using the Anton Paar Revetest® Scratch Tester RST3 instrument. The unreacted samples were tested for progressive loading to identify the minimum load that could generate fracture on unreacted samples without damaging the sample. The constant loading was identified as 40 N for both Divider and Arrester orientations. Furthermore, the scratch length was chosen to be 5 mm. The scratch speed and acoustic emission sensitivity were set as 6.0 mm/min and 9 respectively. Fig. 2 shows the tested unreacted and reacted samples attached to Delrin. Scratch testing was initiated from Delrin towards the rock samples to prevent damage to the testing tip. The results concerning Delrin testing have been excluded from the analysis.

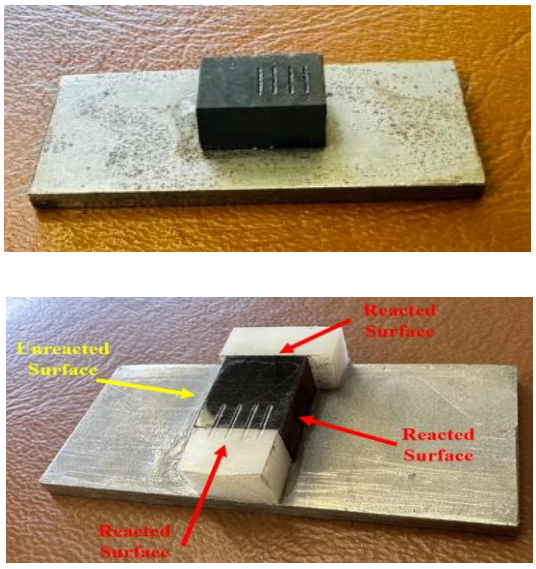

Fig. 2. Eagle Ford (a) unreacted sample, and (b) reacted sample attached to Delrin.

3. RESULTS AND OBSERVATIONS

3.1. Scratch Acoustic Emission

Acoustic emission (AE) signals, obtained directly from the scratch test, provided valuable insights into the mechanical response of the reacted samples during scratching. Notably, the AE readings remains relatively constant within the distance range of 900 µm to 1200 µm from the reacted surface, signifying a predominantly ductile deformation regime during this phase. As the scratch test progressed beyond the aforementioned distance range, a transition from the ductile to the brittle region of the reacted sample was observed, accompanied by discernible peaks in the acoustic emission readings due to surface damage reconnaissance (Stebut et al. 1999). These peaks indicate a shift in material behavior, suggestive of the initiation of brittle fracture events. This observation is highlighted with the representative test (red line) and other tests (gray lines) for the Reacted-Divider direction sample in Fig. 3, where the graphical representation captures the shift from consistent readings in the ductile region to the emergence of distinct peaks in the brittle region.

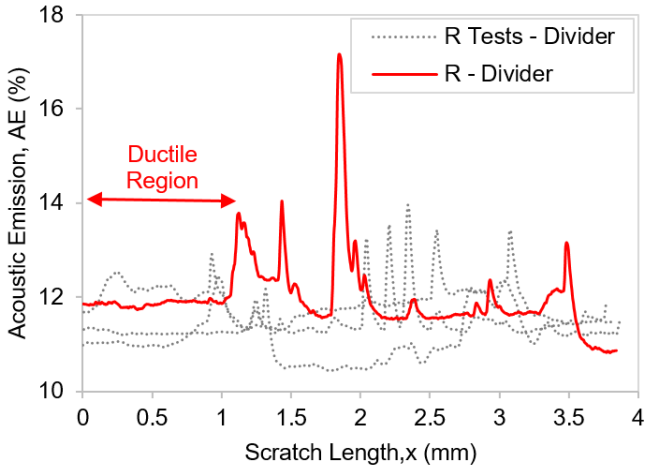

Fig. 3. Acoustic emissions for the reacted divider direction.

3.2. Scratch Tangential Force

In Fig. 4, the tangential force results reveal an intriguing phenomenon in the reacted portion of the shale rock. At the initial stages, up to 150 µm in the Arrester direction and 250 µm in the Divider direction, the tangential force is notably higher. Subsequently, the force decreases until reaching a depth of 900 to 1200 µm. This depth from the reacted surface correlates with the constant acoustic emission signals observed in the previous section. It is important to note that the red line in Fig. 4 represents one reacted test, while the blue line represents one unreacted test and the gray dotted lines represent both reacted and unreacted tests. This distinction correlates with the higher scratch depth observed in the reacted region, indicating greater material compressibility in this region.

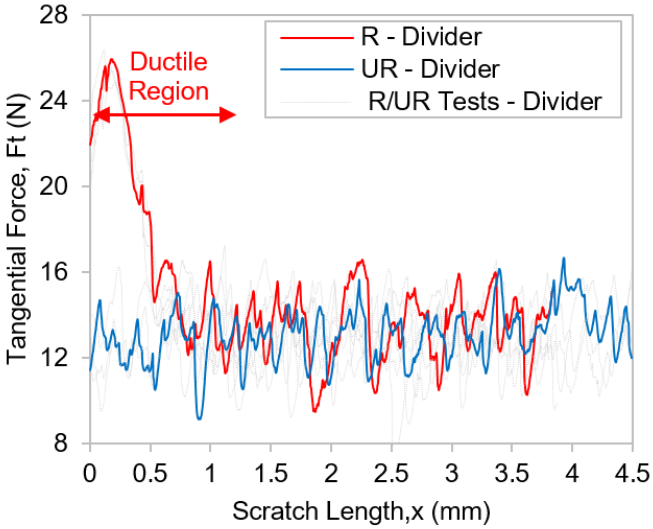

(a)

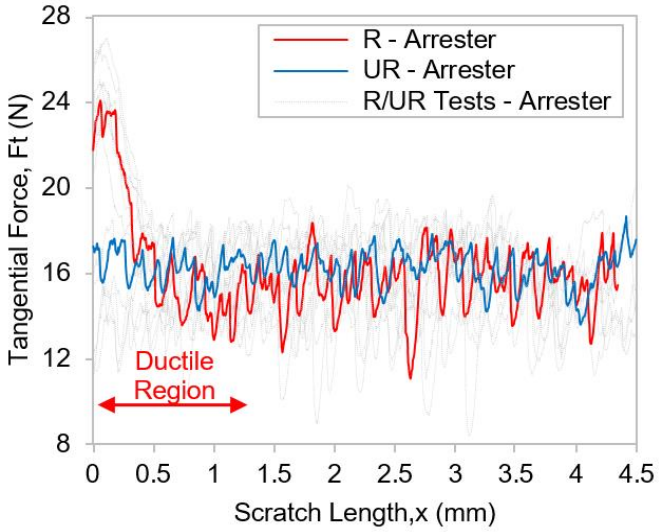

(b)

Fig. 4. Tangential force readings under constant 40 N scratch test loading for (a) divider direction, and (b) arrester direction.

3.3. Scratch Hardness

The primary analysis conducted in this study is based on the hardness data obtained from 40 scratch tests performed under a constant loading of 40 N. Scratch hardness serves as a measure of the material's average response to the contact load applied by the probe. In practical terms, a greater scratch depth indicates a softer material, while a shallower scratch depth suggests a harder material. Two types of scratch hardness are typically utilized: vertical hardness (H_v), which is determined by the vertical load (F_{nm}) and the vertical contact area between the scratch tip and the rock surface (A_P), and scratch hardness (H_s), which is influenced by the transverse load (F_T) and the area of contact projected horizontally (A_{LB}). Both of these areas are dependent on the penetration depth achieved during the scratch test.

Fig. 5 and 6 illustrate the horizontal (red) and vertical (blue) hardness profiles for both reacted (a), and unreacted (b) samples in the Divider, and arrester direction, respectively. The gray dotted lines represents horizontal and vertical hardness for all tests in Divider Direction. Notably, the horizontal hardness curves exhibit greater fluctuation, indicative of material crushing and chipping in both reacted and unreacted samples. Conversely, the vertical hardness curves demonstrate smoother trends, attributed to compression-induced particle rearrangement. While the horizontal and vertical curves for the unreacted sample (dotted lines) follow similar patterns throughout the scratch length, those for the reacted sample (solid lines) exhibit distinct behavior in the first 500 µm, attributable to the ductility of this region. Despite the higher tangential force observed in this region, the increased penetration depth significantly influences the total horizontal hardness due to the pronounced dissolution occurring in this region. During the scratch test, the reacted sample exhibits the lowest hardness in this region, at 500 µm from the reacted surface, coinciding with the observed micro-cracks later shown in Fig. 11 and 13.

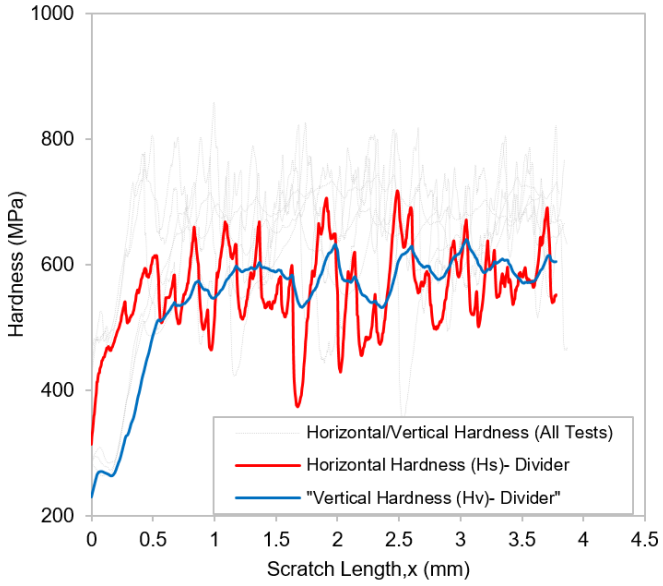

(a)

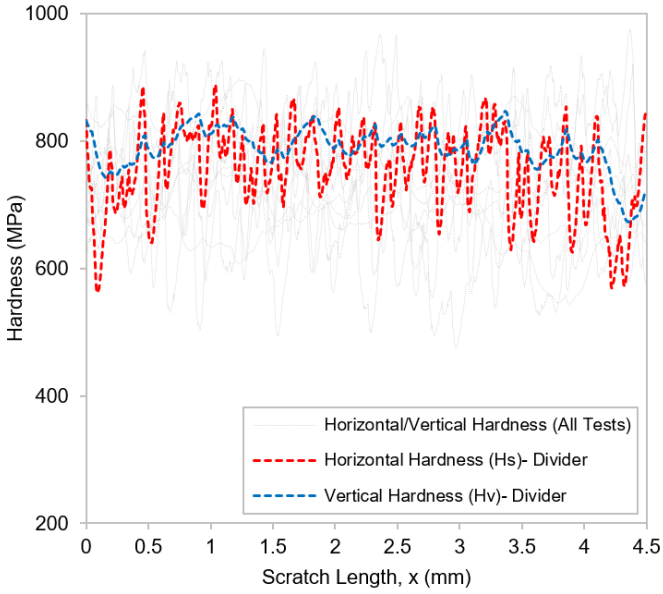

(b)

Fig. 5. Representative curves for horizontal and vertical hardness in the divider direction for (a) reacted sample (solid lines), and (b) unreacted sample (dotted lines).

In the divider direction, the reacted sample demonstrates reduced hardness to a depth of 1000 µm from the reacted surface approximately. Conversely, in the arrester direction (Fig. 6 (a), and (b)), with the aid of the representative curves (solid lines), a noticeable reduction in vertical hardness is observed only within the initial 400 µm, followed by a region of relatively higher hardness in the reacted sample. This phenomenon is attributed to

carbonate precipitation, as previously demonstrated through nanoindentation grid analysis at a depth of 250 µm from the reacted surface (Prakash et al. 2021; Prakash et al. 2022). The influence of the reaction is discernible up to an approximate reaction depth of 900 to 1200 µm in both horizontal hardness profile (red) and vertical hardness profile (blue) for the arrester direction. Furthermore, the representative vertical hardness profile demonstrates a slight reduction compared to the scratch hardness profile observed in the unreacted sample (dotted lines), where the hardness for both horizontal and vertical profiles remain relatively similar.

In the arrester direction, between depths ranging from 1400 to 1500 µm from the reacted surface, a discernible reduction in vertical hardness was noted. Examination under scratch microscopes revealed the formation of deep fractures, as depicted in Fig. 7 (a) and (b). This phenomenon was consistently observed across the majority of scratches conducted on the reacted sample. This phenomenon was consistently observed across the majority of scratches conducted on the reacted sample. As the scratch past the precipitation zone, hardness exhibit a gradual decrease. This trend suggests a transition in the material's mechanical properties, possibly indicating the conclusion of the reaction front or the initiation of a no-reaction zone. Such behavior underscores the dynamic nature of the material's response to the ongoing chemical processes.

In Fig. 8 (a) and (b), the distribution of hardness values is analyzed based on frequency with a focus on the effect of reacted regions on the material properties. The red and black colors represent the divider and arrester directions, respectively, while the solid and dotted lines correspond to reacted and unreacted samples. The term "average hardness" denotes the mean value obtained from hardness measurements, calculated by averaging measurements from multiple scratched within samples using standard statistical methods for both horizontal and vertical hardness. For each direction, eight scratches were conducted on the reacted samples (denoted as R), whereas twelve scratches were performed on the unreacted samples (denoted as UR).

Our analysis reveals that the presence of reacted regions significantly influences the hardness distribution, leading to observed variations compared to unreacted regions. The distribution of average horizontal hardness shows predominant concentrations within the range of 600 – 650 MPa for both unreacted and reacted samples, with the unreacted arrester direction exhibiting the highest frequency in Fig. 8 (a). Contrastingly, the unreacted divider direction demonstrates relatively higher horizontal hardness in the ranges of 650-700 MPa and 700-750 MPa.

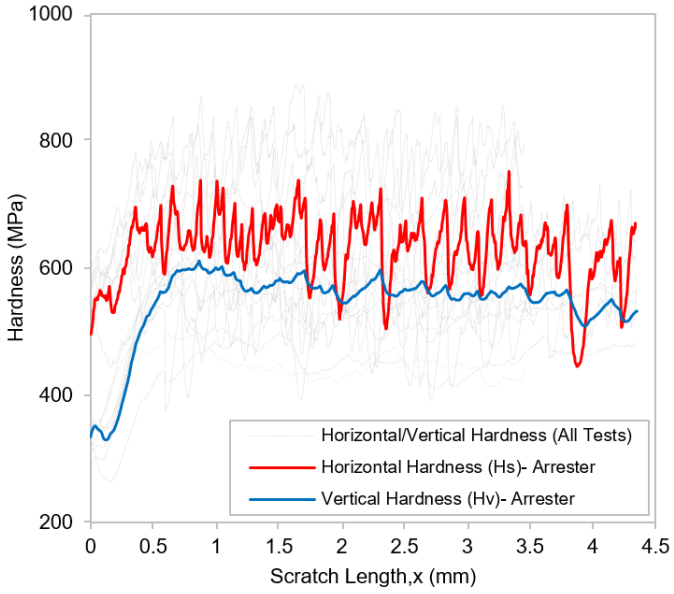

(a)

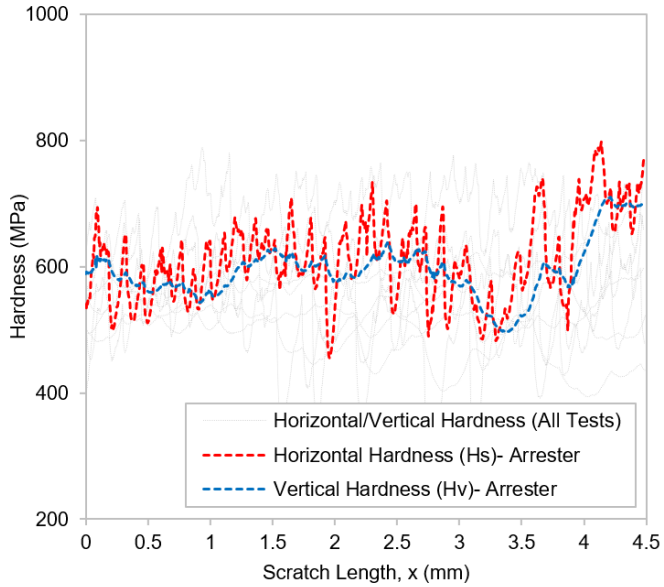

(b)

Fig. 6. Representative curves for horizontal and vertical hardness in the arrester direction for (a) reacted sample (solid lines), and (b) unreacted sample (dotted lines).

In Fig. 8 (b), the arrester direction displays a lower range of average vertical hardness compared to the divider direction. Furthermore, the reacted samples for both arrester and divider directions demonstrate a significantly lower range of vertical hardness, particularly near to the reacted surface (corresponds to 900 to 1200 µm depth from reacted surface). This range varies from 200-250 MPa up to 550-600 MPa for the reacted arrester direction and from 250-300 MPa up to 450-500 MPa for the reacted divider direction.

The vertical-to-horizontal hardness ratio serves as a valuable tool for identifying areas within the material that

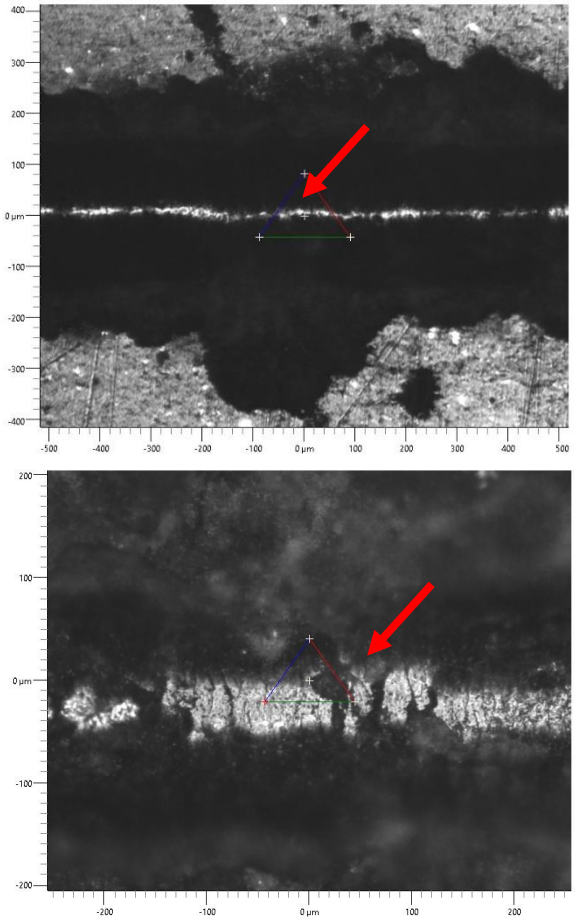

Fig. 7. Cracks formation (red arrow) in the scratch path of the reacted arrester sample (a) 5X microscope, and (b) 10X microscope.

have undergone chemical reactions. This ratio can indicate the material's ability to resist compression and crushing in comparison to its tendency to undergo fracture formation. (Liu et al. 2020).

In the divider direction, as depicted in Fig. 9 (a), the vertical-to-horizontal hardness ratio within the reacted region varies from 0.6 to 1.0 in the vicinity of the reacted surface (Region.1), indicating spatial heterogeneity in the material's mechanical response. This variability suggests tendency towards compression rather than fracture formation in the reacted region. . Beyond a depth of 900 to 1200 µm from the reacted surface, the ratio stabilizes around 1.0 (Region.2), indicating a consistent mechanical response to both vertical and horizontal loading. Conversely, the unreacted sample maintains a constant ratio of approximately 1.0 throughout the scratch length, signifying consistent mechanical behaviour. Similarly, in the arrester direction, as illustrated in Fig. 9 (b), the vertical-to-horizontal hardness ratio demonstrates distinct patterns within the reacted region. Within the initial 800 µm from the reacted surface, the ratio varies from 0.6 to 0.85 (Region.1), suggesting localized variations in mechanical behaviour. Beyond this depth, the ratio stabilizes around 0.85 (Region.2), indicating a consistent mechanical response. In contrast, the unreacted sample exhibits a constant ratio of approximately 0.9 for the entire scratch length, suggesting consistent mechanical behavior unaffected by chemical reactions.

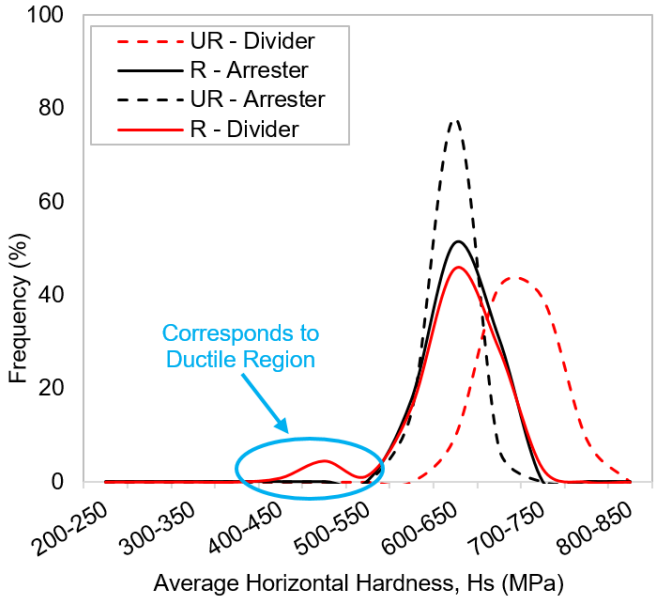

(a)

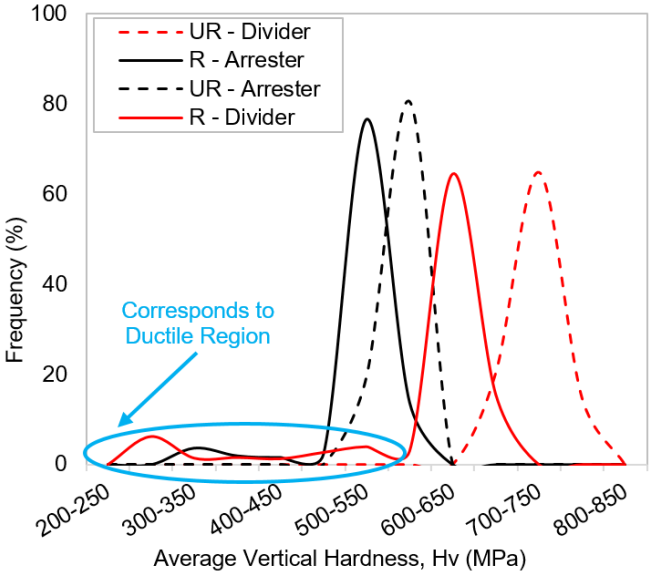

(b)

Fig. 8. Average hardness (a) horizontal, and (b) vertical for reacted and unreacted samples.

Understanding these relationships is paramount for predicting the material's response to external loads and evaluating its structural integrity in practical applications. It is noteworthy that this comparison ratio is derived from the average values obtained from the analysis conducted for both divider and arrester directions.

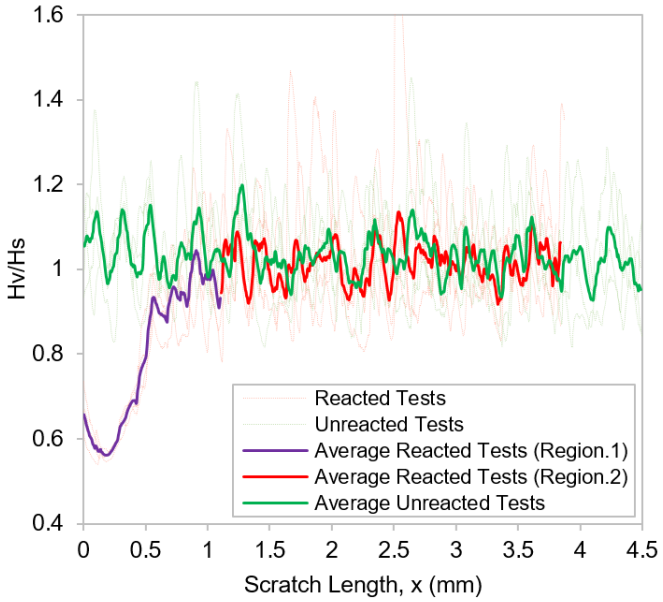

(a)

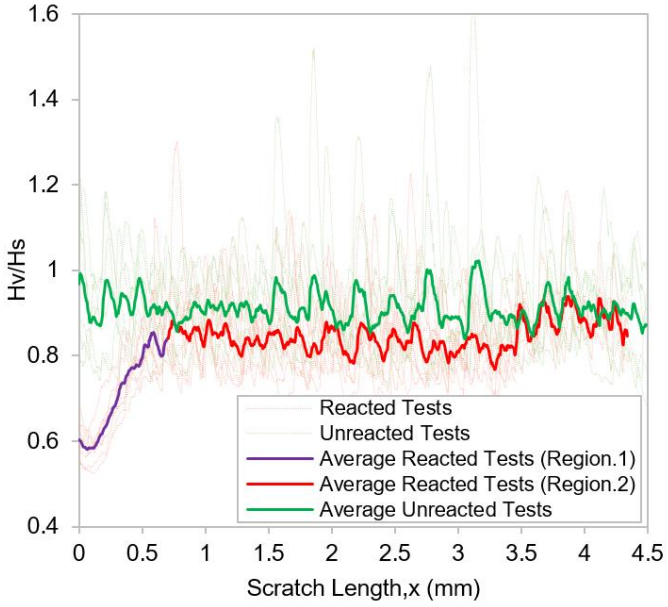

(b)

Fig. 9. Vertical hardness to horizontal hardness (Hv/Hs) ratio for reacted and unreacted samples in (a) Divider, and (b) Arrester directions.

4. FURTHER DISCUSSION

4.1. Fracture Pattern and Cracks

In the reacted sample, notable differences are observed in the fracture pattern in the reacted region (R) compared to regions distant from the reacted surface (UR) (> 1500 µm). Moreover, a higher incidence of micro-fractures is evident between the main fracture patterns, particularly in the Divider direction (yellow arrows). This observation correlates with the depth of reaction being greater in the Divider direction compared to the Arrester direction, a phenomenon attributed to the orientation of bedding planes. Fig. 10 (a) and (b) illustrate the scratch paths for the reacted sample, illustrating regions adjacent to (upper image), and distant from the reacted surface (lower image). A red rectangular bar in the top image represents the reacted surface. Conversely, in the reacted sample, the initiation of material crushing occurs within the reacted region (ductile fractures), contributing to a distinctive fracture pattern that deviates from the region far from the reacted surface.

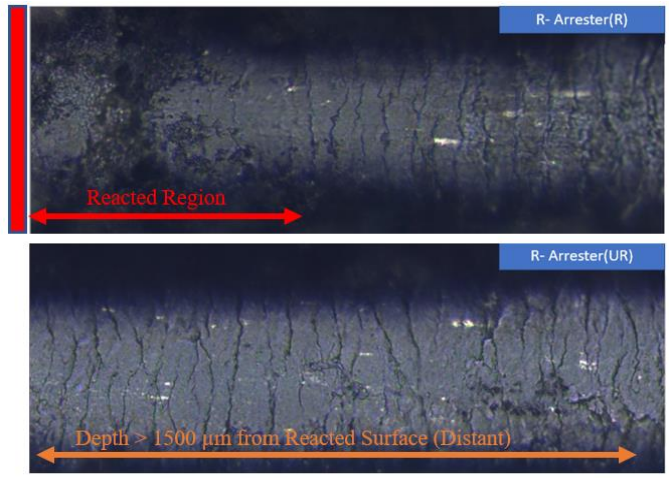

(a)

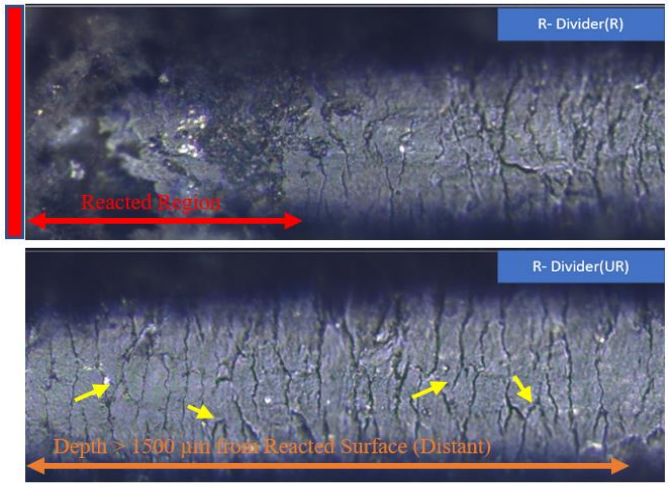

(b)

Fig. 10. Fracture pattern comparison between reacted sample close to the reacted surface (R) and reacted sample far from the reacted surface (UR) samples in both (a) arrester, and (b) divider directions.

The structural vulnerability of the dissolution region can result in the formation of fractures, channels, and gaps between the dissolution and precipitation zones. This phenomenon, illustrated by observed microcracks, aligns with findings from studies on similar geomaterials exposed to reactive brine (Li et al., 2015). This is especially evident given the prevalence of observed cracks below location of the micro-scratch test, as depicted in Fig. 11 and 12. In these figures, post-scratch test cracks perpendicular to the scratch direction were observed within the reacted region for both directional

orientations (Divider and Arrester). In Fig. 11, a crack labelled as (1), indicated with a yellow arrow, was observed at 400 µm from the reacted surface in the Divider Direction. In Fig. 12, cracks labelled as (1), (2), and (3) were observed at distances of 140 µm, 200 µm, and 280 µm from the reacted surface in the Arrester direction.

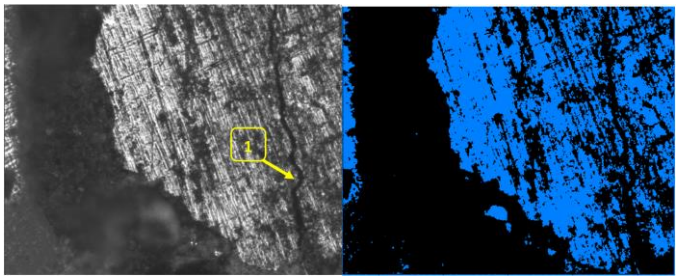

Fig. 11. Reacted divider direction, showing a crack at 400 µm (1) from the reacted surface, as indicated by yellow arrow.

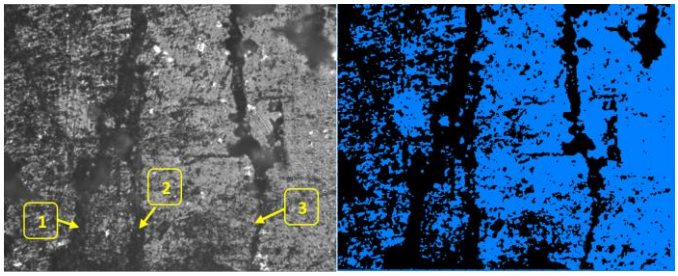

Fig. 12. Reacted arrester direction, showing cracks at 140 µm (1), 200 µm (2), and 280 µm (3) from the reacted surface, as indicated by yellow arrows.

4.2. Dissolution and Precipitation Dynamics

To characterize the dissolution and precipitation phases across distinct zones, variations in material phases within Eagle Ford samples need to be understood. Calcite dissolution emerges as the primary reaction at the surface, as outlined by the following chemical equations (Prakash et al., 2022):

$$CO_2(g) \leftrightarrow CO_2(aq) \quad (1)$$

$$CO_2(aq) + H_2O \leftrightarrow H_2CO_3 \quad (2)$$

$$H_2CO_3 + CaCO_3 \leftrightarrow Ca^{2+} + 2HCO_3^- \quad (3)$$

Eq. (1) signifies the dissolution of CO_2 in brine, which influenced by temperature and pressure, initiates carbonic acid formation Eq. (2). Subsequently, calcite dissolves into the resultant solution Eq. (3). The increased concentration of dissolved calcium and carbonate ions in the aqueous solution leads to a state of supersaturation, thereby facilitating precipitation processes. Calcium carbonate is then deposited within the precipitation zone, as per the following reactions (Bachu et al., 1994; Gunter et al., 1997; Le Gallo et al., 2002; Rosenbauer et al., 2005):

$$H_2CO_3 \leftrightarrow H^+ + HCO_3^- \quad (4)$$

$$HCO_3^- \leftrightarrow H^+ + {CO_3}^{2-} \quad (5)$$

$$Ca^{2+} + {CO_3}^{2-} \leftrightarrow CaCO_3 \downarrow \quad (6)$$

Eq. (4) and Eq. (5) denote the generation of carbonate ions through the dissociation of carbonic acid. These carbonate ions subsequently interact with dissolved Ca^{2+} (generated through dissolution) in the brine, leading to the formation of calcium carbonate precipitate as Eq. (6).

4.3. The Effect of Reaction on Brittleness

Brittle materials store strain energy mainly through elastic deformation, which is quickly released upon failure. In contrast, ductile materials have a limited ability to store strain energy and slowly release it through plastic deformation as previously mentioned in Hernandez-Uribe et al. (2017). Differences in the volume affected by scratch testing between reacted and unreacted regions necessitate relying on hardness curves rather than tangential force to represent brittleness.

Upon reviewing the representative curves of the reacted samples in both the divider and arrester directions, depicted in Fig. 5 (a) and 6 (a) for horizontal and vertical hardness, several notable observations arise. Specifically, the fluctuation appears smoother at the onset of the hardness curves within the reacted region. This smoother transition can be attributed to the material's heightened deformability and compressibility compared to the unreacted portion, situated farther from the reacted edge. Additionally, with the aid of the top images in Fig. 10 (a) and (b), it becomes evident that fracture formation initiates in the precipitation zone (approximately after 500 µm from the reacted surface).

Finally, in the ductile region, as more gradual change in hardness over distance was observed, indicative of a lower rate of change of vertical to horizontal hardness ($\Delta H/\Delta X$), where H represents H_v/ H_s. This lower rate suggests a slower transition in hardness along the scratch path, reflecting the material's ability to deform plastically without abrupt changes in hardness. Conversely, in the brittle region, where the material is more prone to fracturing, a higher rate of change in hardness over distance may be observed. The higher rate signifies a more rapid variation in hardness, indicative of brittle behavior characterized by sudden and significant changes in hardness as cracks propagate. Therefore, the rate of change of vertical to horizontal hardness ratio can serve as an indicator of brittleness, with higher rates potentially

indicating greater brittleness and lower rates suggesting more ductile behavior. These observations are depicted in Fig. 13, where the divider direction of the reacted sample was considered. The dotted red lines represent the moving average calculated every 20 data points.

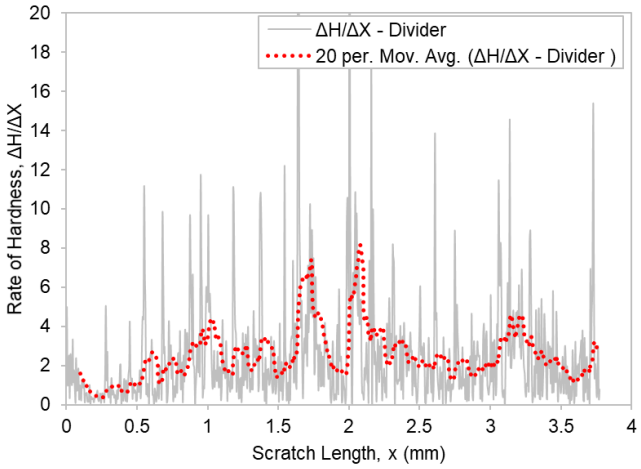

Fig. 13. Rate of change of hardness along scratch path for divider reacted sample.

5. CONCLUSIONS

The scratch hardness analysis conducted in this study, based on 40 scratch tests performed under constant loading, provides valuable insights into the micro-mechanical properties of the carbonate-rich shale rock samples after being exposed to CO_2-rich brine under high pressure and high-temperature conditions. Scratch hardness serves as a metric for assessing the material's response to contact loads, with greater scratch depths indicating softer materials and shallower depths indicating harder materials. Two types of hardness were computed, vertical (H_v) and scratch (H_s), which offer complementary perspectives on the material's mechanical behavior, with variations influenced by factors such as loading direction with respect to bedding planes and penetration depth. In the divider direction, the reacted sample exhibits reduced hardness compared to the unreacted sample up to 900 µm to 1200 µm from the reacted surface. Conversely, in the arrester direction, the reacted sample displays a distinct pattern characterized by an initial reduction in hardness followed by a region of relatively higher hardness attributed to carbonate precipitation.

The observed variations underscore the complex interplay between chemical reactions, microstructural changes, and mechanical properties in shale rocks. Additionally, the analysis of the vertical-to-horizontal hardness ratio reveals spatial heterogeneity in the material's mechanical response, with differences attributed to microstructural features and reaction-induced alterations. These findings contribute to a deeper understanding of the coupling between chemical reactions and mechanical alterations in shale rock at the microscale. This study elucidates how these coupled processes influence the behavior of shale under external loads, providing valuable insights for assessing structural integrity in practical applications. The scratch acoustic emission data revealed a transition from predominantly ductile to brittle behavior within the reacted sample. Consistent acoustic emission readings within the region spanning from the reacted edge up to approximately 900 µm to 1200 µm indicated ductile behavior, while discernible peaks beyond this range suggested the initiation of brittle fracture events.

The tangential force readings illustrate a distinctive trend in the reacted portion of the shale rock. Initially, higher forces are observed, followed by a subsequent decrease with increasing depth. This phenomenon aligns with consistent acoustic emission signals and is indicative of evolving mechanical responses governed by porosity changes. As when conducting a scratch test on a ductile material and observing both higher tangential force and greater penetration depth. The material exhibits plastic deformation, indicating its ability to undergo shape changes without fracturing immediately. Additionally, the tool penetrates more deeply, implying favourable workability and plastic flow within the material.

The reaction has significantly altered the material's properties, rendering it more ductile and deformable. This transformation is evident from the smoother transitions observed in hardness curves and the initiation of fractures beyond the reacted region which included dissolution and precipitation zones. Furthermore, the rate of change of vertical to horizontal hardness ratio serves as a robust indicator of this shift, with lower rates indicating enhanced ductility and slower transitions in hardness along the scratch path. Conversely, higher rates signify increased brittleness, characterized by abrupt changes in hardness as cracks propagate.

In conclusion, this study highlights the mechanical response of carbonate-rich shale rocks exposed to CO2-rich brine under elevated temperature and pressure conditions. By advancing our comprehension of shale's mechanical properties and responses to these operational conditions, the micro-scratch testing methodology developed in this work lays the groundwork for future investigations into the interplay between chemical and mechanical effects.

ACKNOWLEDGEMENT

The authors gratefully acknowledge the support provided by the National Science Foundation (NSF) through

Award 2045242, which facilitated the completion of this study.

REFERENCES

1. Bachu, S., Gunter, W. D., & Perkins, E. H. (1994). Aquifer disposal of CO2: hydrodynamic and mineral trapping. *Energy Conversion and management*, *35*(4), 269-279.
2. Bažant, Z. P., & Kazemi, M. T. (1990). Size effect in fracture of ceramics and its use to determine fracture energy and effective process zone length. *Journal of the American Ceramic Society*, *73*(7), 1841-1853.
3. Burnside, N. M., Shipton, Z. K., Dockrill, B., & Ellam, R. M. (2013). Man-made versus natural CO2 leakage: A 400 ky history of an analogue for engineered geological storage of CO2. *Geology*, *41*(4), 471-474.
4. Dubey, V., Abedi, S., & Noshadravan, A. (2020, June). Experimental Characterization of Microcrack-Induced Damage Behavior in Shale Rocks using Miniature Tensile Module. In *ARMA US Rock Mechanics/Geomechanics Symposium* (pp. ARMA-2020). ARMA.
5. Gunter, W. D., Perkins, E. H., & Hutcheon, I. (2000). Aquifer disposal of acid gases: modelling of water–rock reactions for trapping of acid wastes. *Applied geochemistry*, *15*(8), 1085-1095.
6. Gunter, W. D., Wiwehar, B., & Perkins, E. H. (1997). Aquifer disposal of CO2-rich greenhouse gases: extension of the time scale of experiment for CO2-sequestering reactions by geochemical modelling. *Mineralogy and petrology, 59*(1-2), 121.
7. Helmer, G. S., Sulem, J., Ghabezloo, S., Rohmer, J., & Hild, F. (2014, May). Experimental evaluation of the fracture toughness on a limestone. In *ISRM EUROCK* (pp. ISRM-EUROCK). ISRM.
8. Hernandez-Uribe, L. A., Aman, M., & Espinoza, D. N. (2017). Assessment of mudrock brittleness with micro-scratch testing. *Rock Mechanics and Rock Engineering, 50*, 2849-2860.
9. Hucka, V., & Das, B. (1974, October). Brittleness determination of rocks by different methods. In *International Journal of Rock Mechanics and Mining Sciences & Geomechanics Abstracts* (Vol. 11, No. 10, pp. 389-392). Pergamon.
10. Kabir, P., Ulm, F. J., & Akono, A. T. (2017). Rate-independent fracture toughness of gray and black kerogen-rich shales. *Acta Geotechnica, 12*, 1207-1227.
11. Le Gallo, Y., Couillens, P., & Manai, T. (2002, March). CO2 sequestration in depleted oil or gas reservoirs. In *SPE International Conference and Exhibition on Health, Safety, Environment, and Sustainability*? (pp. SPE-74104). SPE.
12. Li, Q., Lim, Y. M., Flores, K. M., Kranjc, K., & Jun, Y. S. (2015). Chemical reactions of portland cement with aqueous CO2 and their impacts on cement's mechanical properties under geologic CO2 sequestration conditions. *Environmental science & technology*, *49*(10), 6335-6343.
13. Mart, J., Zeng, Q., & Xu, S. (2020). Is scratch test proper to characterize microstructure and mechanical properties of cement-based materials? The effects of loading level and routine. *Cement and Concrete Research, 133*, 106072.
14. Martogi, D., Mahgoub, S. A., Noshadravan, A., & Abedi, S. (2023). Estimating mode II fracture energy of rocks using the scratch test and phase field modeling. *Acta Geotechnica*, 1-17.
15. Martogi, D., Vaibhav, A., Noshadravan, A., & Abedi, S. (2020, October). Approximation of rock fracture toughness using scratch test and phase-field modeling approach. In *SPE Annual Technical Conference and Exhibition*? (p. D041S058R002). SPE.
16. Meng, F., Zhou, H., Zhang, C., Xu, R., & Lu, J. (2015). Evaluation methodology of brittleness of rock based on post-peak stress–strain curves. *Rock Mechanics and Rock Engineering, 48*, 1787-1805.
17. Minardi, A., Stavropoulou, E., Kim, T., Ferrari, A., & Laloui, L. (2021). Experimental assessment of the hydro-mechanical behaviour of a shale caprock during CO2 injection. *International Journal of Greenhouse Gas Control, 106*, 103225.
18. Outlook, A. E. (2016). Early Release: Annotated Summary of Two Cases. *Annual Energy Outlook*, 2016.
19. Pokrovsky, O. S., Golubev, S. V., & Schott, J. (2005). Dissolution kinetics of calcite, dolomite and magnesite at 25 C and 0 to 50 atm pCO2. *Chemical geology, 217*(3-4), 239-255.
20. Prakash, R., Mahgoub, S. A., & Abedi, S. (2023). Chemo-mechanical Alteration of Silicate-Rich Shale Rock after Exposure to CO2-Rich Brine at High Temperature and Pressure. *Rock Mechanics and Rock Engineering*, 1-17.
21. Prakash, R., Nguene, P. C. K., Benoit, D., Henkel, K., & Abedi, S. (2021). Assessment of local phase to mechanical response link: application to the chemo-mechanical identification of rock phases subjected to reactive environments. *Journal of Natural Gas Science and Engineering, 89*, 103857.
22. Prakash, R., Nguene, P. C. K., Noshadravan, A., & Abedi, S. (2022). Chemical reactions of carbonate-rich mudstones with aqueous CO2 and their impacts on rock's local microstructural and chemo-mechanical properties. *Journal of Natural Gas Science and Engineering, 103*, 104587.
23. Prakash, R., Kana Nguene, P., Seers, T. D., Noshadravan, A., & Abedi, S. (2019, June). Chemo-mechanical investigation of CO2-fluid-rock interaction in CO2 storage and CO2-EOR processes in unconventional reservoirs. In *ARMA US Rock Mechanics/Geomechanics Symposium* (pp. ARMA-2019). ARMA.
24. Richard, T., Detournay, E., Drescher, A., Nicodeme, P., & Fourmaintraux, D. (1998, July). The scratch test as a means to measure strength of sedimentary rocks. In *SPE/ISRM rock mechanics in petroleum engineering* (pp. SPE-47196). SPE.
25. Richard, T., Dagrain, F., Poyol, E., & Detournay, E. (2012). Rock strength determination from scratch tests. *Engineering Geology, 147*, 91-100.
26. Rosenbauer, R. J., Koksalan, T., & Palandri, J. L. (2005). Experimental investigation of CO2–brine–rock interactions at elevated temperature and pressure: Implications for CO2 sequestration in deep-saline aquifers. *Fuel processing technology, 86*(14-15), 1581-1597.
27. Smith, D. G., & Chowdary, M. (1975). The fracture toughness of slip-cast fused silica. *Materials Science and Engineering, 20*, 83-88.

28. Sun, Z., Espinoza, D. N., & Balhoff, M. T. (2016). Discrete element modeling of indentation tests to investigate mechanisms of CO2-related chemomechanical rock alteration. *Journal of Geophysical Research: Solid Earth, 121*(11), 7867-7881.
29. Von Stebut, J., Lapostolle, F., Bucsa, M., & Vallen, H. (1999). Acoustic emission monitoring of single cracking events and associated damage mechanism analysis in indentation and scratch testing. *Surface and coatings technology, 116*, 160-171.